Applied Catalysis B: Environmental 237 (2018) 251–262

Contents lists available at ScienceDirect

Applied Catalysis B: Environmental

journal homepage: www.elsevier.com/locate/apcatb

Study of Ag promoted Fe_2O_3@CeO_2 as superior soot oxidation catalysts: The role of Fe_2O_3 crystal plane and tandem oxygen delivery

Houlin Wang[a], Baofang Jin[b], Haobo Wang[a], Ningning Ma[a], Wei Liu[a], Duan Weng[b], Xiaodong Wu[b], Shuang Liu[a,*]

[a] School of Materials Science and Engineering, Ocean University of China, Qingdao 266100, China
[b] Key Laboratory of Advanced Materials of Ministry of Education of China, School of Materials Science and Engineering, Tsinghua University, Beijing 100084, China

ARTICLE INFO

Keywords:
Fe_2O_3
Ag/CeO_2
Soot oxidation catalyst
Crystal plane
Tandem oxygen delivery

ABSTRACT

In this work, model α-Fe_2O_3 catalysts with different morphologies were synthesized to investigate crystal plane effects on soot oxidation. The results revealed that the electron-rich state of Fe_2O_3 {113} planes conferred them more surface O_x^- and thus better catalytic performance than the {014} and {012} planes. Surface grafting of a polycrystalline CeO_2 layer onto Fe_2O_3 gave rise to Fe_2O_3@CeO_2 catalysts with drastically increased oxygen utilization. More importantly, by loading Ag nano-particles on the surface of Fe_2O_3@CeO_2, a tandem oxygen delivery route was opened, resulting in strong O_x- generation/regeneration ability and superior low temperature soot oxidation activity. These Ag/Fe_2O_3@CeO_2 catalysts overwhelmed the nano-cubic Ag/CeO_2 in both catalyst cost and activity, making them very promising for application in catalyzed gasoline particulate filters (CGPFs).

1. Introduction

The market for gasoline-powered vehicles has been in prosperity for decades. In order to meet the needs of high power output and low CO_2 emission simultaneously, gasoline direct injection (GDI) engines resurfaced and boomed these years. To overcome the side effect of increased particle number (PN) emissions caused by GDI engines, special aftertreatment systems including catalyzed gasoline particulate filters (CGPFs) were designed, through which the exhaust particulate matter (mainly soot) could be trapped and burnt out catalytically [1]. Pt-based materials have long been proven efficient diesel oxidation catalysts [2], but the special working condition of CGPF (low O_2 concentration and almost no NO_x) disfavors the application of platinum [3,4]. In contrast, ceria-based materials, especially nano-cubic Ag/CeO_2-based catalysts are highly active and thermally stable for soot oxidation in CGPF working condition [5–8]. Therefore, these inexpensive materials can be substitution for platinum, as long as they overcome the following problems: On one hand, it is difficult for Ag/CeO_2 to oxidize soot at low temperatures (below 300 °C) [6]. This is, however, a common condition for the exhaust in CGPF which is cooled by the upstream three-way catalyst (TWC) [1]. On the other hand, due to insufficient active oxygen supply and dynamic changes in oxygen vacancies, Ag/CeO_2 deactivates during soot oxidation and becomes inert gradually [7,9]. In this sense, further work is needed to develop catalysts with higher practicability than Ag/CeO_2.

According to previous studies, the key factors determining low temperature soot catalytic oxidation center on catalysts' ability of delivering sufficient O_x^- (especially O_2^-) onto soot particles [6,10,11]. These O_x^- species come either from gaseous O_2 (surface spillover), or from catalyst bulk oxygen (bulk diffusion) [7]. Given the low O_2 concentration in CGPF limits the first route, choosing materials with high bulk oxygen utilization is a promising way to develop CGPF catalysts. Iron oxide (e.g. Fe_2O_3) is such a choice. Being a commercial fuel-borne soot oxidation catalyst overwhelming CeO_2 [12,13], Fe_2O_3 shows ultrahigh bulk oxygen capacity and very low cost. The main drawback of Fe_2O_3 is its low oxygen conducting rate, which limits its application in low-temperature reactions. Recently, Machida et al. observed that CeO_2 could act as the gateway of oxygen release/storage for Fe_2O_3 [14]. As a consequence, Fe_2O_3 particles grafted with CeO_2 exhibited high oxygen utilization. Similar results have also been reported by Zhang [15], Galvita [16], Cheng [17] and Luo [18] et al. in dealing with different catalytic oxidation reactions. Moreover, our recent studies indicated that silver nano-particles acted as "oxygen pump" that enhanced the oxygen availability of CeO_2 significantly [6,7]. Inspired by these works, a new generation core-shell catalysts can be designed: (1) Fe_2O_3 acting as the inner core, providing sufficient bulk oxygen, (2) CeO_2 particles encapsulating Fe_2O_3 to accelerate its oxygen deliver rate and (3) Ag impregnating over CeO_2, which can further improve the oxygen utilization of the system.

Besides catalyst component, another nonnegligible factor that

* Corresponding author.
E-mail address: lius@ouc.edu.cn (S. Liu).

https://doi.org/10.1016/j.apcatb.2018.05.093
Received 17 March 2018; Received in revised form 28 April 2018; Accepted 30 May 2018
Available online 31 May 2018

influences catalysts' behavior is the exposure of specific crystalline planes. Surface atoms on different planes of a solid are usually in different coordination environments, therefore offering different activation capabilities to reactants. For instance, by controlling ceria to expose planes like {110} and {100} rather than the thermally stable {111} planes, effective oxygen providers boosting low-temperature soot oxidation were obtained [6,19]. Similarly, Fe_2O_3 could be induced to expose thermally unfavorable facets like {012}, {113} and {134}, which resulted in catalysts with high CO oxidation ability [20,21]. Nevertheless, the relationship between Fe_2O_3 planes and their soot oxidation behavior has not been understood yet. Once this relationship is unveiled, by combining the inner Fe_2O_3 core with designed morphology and the Ag/CeO_2 shell materials, catalysts with optimized soot oxidation activity can be achieved.

Based on the above design, we report the synthesis of Ag promoted $Fe_2O_3@CeO_2$ catalysts. By adjusting the morphology of the inner Fe_2O_3 core, catalysts with superior low-temperature soot oxidation activity were obtained. Further exploration on reaction mechanism confirmed the influences of different Fe_2O_3 planes and tandem oxygen delivery on catalysts' performance.

2. Experimental section

2.1. Catalyst synthesis

Detailed synthesis processes are shown in the Supporting Information (Fig. S1). Generally, monodisperse iron oxides with different morphologies (cubes: "**-C**", rhombohedrons: "**-R**" and octadecahedrons: "**-O**") were synthesized via the hydrothermal methods and denoted as **Fe-C**, **Fe-R** and **Fe-O,** respectively [22–25]. Fe_2O_3 catalysts coated with a polycrystalline CeO_2 shell ($Fe_2O_3@CeO_2$, denoted as **Fe@Ce**) were obtained via a chemical precipitation [26]. Silver species (5 wt.%) were loaded on these supports by incipient wetness impregnation and subsequent calcination. After Ag impregnation, the Fe_2O_3 and $Fe_2O_3@CeO_2$ catalysts were denoted as **Ag/Fe** and **Ag/Fe@Ce**, respectively.

2.2. General characterizations

Sample morphology was observed through a field emission scanning electron microscope (MERLIN VP Compact, ZEISS, Germany), a transmission electron microscopy (JEOL 2100 with an accelerating voltage of 200 kV and a point resolution of 0.19 nm) and N_2 adsorption/desorption isotherms at 77 K (JW–BK122 F, Beijing JWGB, China). Powder X–ray diffraction (XRD) patterns were performed on a diffractometer (D8 ADVANCE, Bruker, Germany) employing Cu–Ka radiation (λ = 0.15418 nm). X–ray photoelectron spectra (XPS) were recorded on an ESCALAB 250 Xi system equipped with monochromatic Al K_α (1486.6 eV) X–ray source. The binding energy of C 1*s* (284.8 eV) was used as an internal standard. Elemental analysis (Fe and Ce) by ICP-AES was performed using an Agilent 725. Raman spectra were obtained through a LabRAM HR 800 (HORIBA Jobin Yvon, France) with a detective laser of 532 nm.

2.3. Activity measurements

Printex–U (diameter 25 nm, surface area 100 m^2/g, Degussa), whose morphology and combustion behavior were reportedly similar to GDI soot [27,28], was chosen as the model soot. Before each test, the catalyst and soot were firstly mixed, either in a "tight" or a "loose" contact mode. A "tight" contact (grinding 10 mg of soot and 100 mg of catalyst in an agate mortar for 5 min) leads to homogenous mixtures of catalyst and soot particles, which makes the evaluation of catalyst-soot contact points possible [6]. Meanwhile, the practical condition in particulate filters resembles the "loose" contact mode (mixing soot and catalyst with a spatula for 2 min) [29]. The soot-catalyst mixture was further diluted with 300 mg of silica pellets to minimize the effect of hot spots, and then sandwiched by quartz wool and placed in a vertical fixed–bed quartz reactor. A gas mixture of (5% H_2O)/1% O_2/N_2 (500 ml/min, GHSV = 100,000 h^{-1}) was fed (simulation of CGPF working condition) [6]. Two types of test methods were applied in this work:

(1) Temperate-programmed oxidation (TPO) process at a constant heating rate (5 °C/min) from room temperature (RT) to 700 °C. The results reflected the catalyst activity roughly.
(2) Isothermal reactions of different catalysts at 250 °C, 275 °C, 300 °C or 325 °C (the soot conversion < 10%). The results revealed the catalysts' behavior in detail. Normalized CO_x production was obtained via dividing the CO_x concentration by the number of available catalyst-soot contact points (see the Supporting Information for details).

The concentration of CO_2 and CO in the outlet gas was monitored by an infrared spectrometer (Thermo Nicolet iS10). Some of these tests (especially the isothermal reactions) were repeated at least twice to ensure the reproducibility of the results.

2.4. Oxygen utilization evaluation

In this work, H_2 temperature–programmed reduction (H_2-TPR) and oxygen storage capacity (OSC) tests were applied to evaluate the dynamic oxygen utilization of different catalysts. Detailed test procedures can be found in the Supporting Information. Generally, H_2-TPR was carried out on a Micromeritics AutoChem II 2920. To investigate the catalyst utility of O_x^- as well as catalysts' redox stability, we also developed cycled TPR tests with pre-oxidation and H_2 reduction performed repeatedly [6–8]. OSC was measured on a thermogravimetric (TG) analyzer (METTLER Toledo) with a dual-supply flow system. During the tests, oxygen gas and reductive hydrogen gas are alternately introduced into the TG system, and the mass changes of the samples were then measured.

3. Results

3.1. Solid properties

Morphologies of the catalysts are illustrated in Fig. 1. As shown in Fig. 1a, e and 1i, Fe-C, Fe-R and Fe-O consisted of monocrystalline nano-polyhedrons (cubes, rhombohedrons and octadecahedrons) with uniform sizes of ~45 nm, ~60 nm and ~65 nm, respectively. Based on the results of HRTEM and previous studies, Fe-C with a dihedral angle of 86° selectively exposed the {012} crystal planes [22], while Fe-R was completely enclosed by the {014} facets [23,24]. As for Fe-O, it exposed twelve clean-cut {113} facets and six relatively small {014} facets [24,25]. Silver species over all the Ag/Fe_2O_3 catalysts (Ag/Fe) were presented in form of metallic Ag particles with diameters of 3–10 nm (see Fig. 1b, f and j).

After ceria coating, all the Fe_2O_3 samples were covered with an 8~10 nm thick polycrystalline CeO_2 layer (Fig. 1c, g and k). Further impregnation of silver onto this CeO_2 layer led to the formation of nano-Ag particles smaller than 3 nm (Fig. 1d, h and l). Ag species on CeO_2 exhibited much better dispersion than those on Fe_2O_3, which was attributed to the high stability of Ag on CeO_2 caused by a strong Ag-CeO_2 bonding effect [30]. As shown in Table 1, all the crystallite sizes data obtained from SEM/TEM were reconfirmed by XRD.

Fig. 2 shows the powder XRD patterns of the catalysts. All of them exhibited high crystallinity and typical hexagonal phase of α-Fe_2O_3. All the ceria-containing catalysts (Fe@Ce and Ag/Fe@Ce) showed typical cubic fluoride CeO_2 crystal phase. As shown in Table 1, their CeO_2 lattice constants were smaller than stantard ceria (0.5411 nm), indicating the formation of solid solutions ($r_{Fe3+} < r_{Ce4+}$) [15,16]. Meanwhile, according to the XAFS results reported by Machida et al.

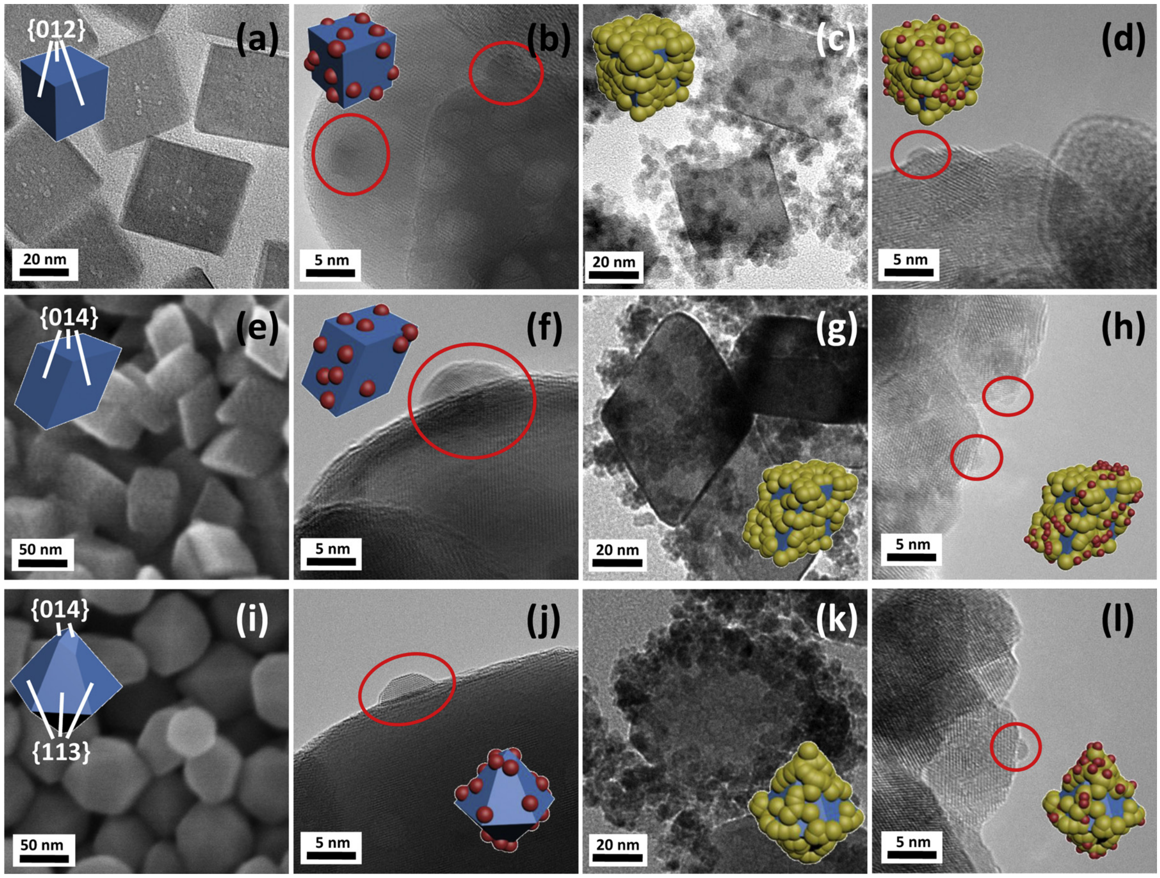

Fig. 1. Typical SEM and HRTEM images of (a) Fe-C, (b) Ag/Fe-C, (c) Fe@Ce-C, (d) Ag/Fe@Ce-C, (e) Fe-R, (f) Ag/Fe-R, (g) Fe@Ce-R, (h) Ag/Fe@Ce-R, (i) Fe-O, (j) Ag/Fe-O, (k) Fe@Ce-O and (l) Ag/Fe@Ce-O. Silver nano-particles were marked with red circles. Fe_2O_3, CeO_2 and Ag were represented by blue, yellow and red polyhedrons in the models, respectively (For interpretation of the references to colour in this figure legend, the reader is referred to the web version of this article).

[14], for Fe_2O_3-CeO_2 samples consisiting of CeO_2 particles supported on Fe_2O_3, only the Fe ions near the interface boundary can dissolve into CeO_2 structure. In this sense, it is supposed that the Fe-in-CeO_2 solid solutions enriched only at the Fe_2O_3-CeO_2 interfacial region. Clearly, Fe@Ce-C and Ag/Fe@Ce-C exhibited smaller CeO_2 lattice constants than other catalysts, implying the abundance of Fe_2O_3-CeO_2 interface in cubic (-C) catalysts. Besides Fe_2O_3 and CeO_2, the diffraction peaks at $2\theta = 38.2°$ and $44.3°$ over Ag/Fe and Ag/Fe@Ce catalysts were attributed to metallic silver [6,7]. For all the samples, no traces of Ag_xO, $FeCeO_3$, $FeCe_2O_4$ and other Fe-based impurities (Fe_3O_4, $Fe(OH)_3$, and FeOOH, etc.) could be detected.

Based on the above structural information, it was suggested that the designed Ag supported α-Fe_2O_3@CeO_2 core-shell structure (Ag/Fe@Ce) had been successfully built.

Quantitative porous structure information of the catalysts is listed detailedly in Table 1. Since all the catalysts were based on nonporous monodisperse Fe_2O_3 nano-particles, their external surface areas (S_{Ext}, obtained from the N_2 adsorption behavior of mesopores with diameters

Table 1
Summary of structure data for the catalysts.

Catalyst	S_{Ext} (m^2/g)[a]	CeO_2 crystallite size (nm)[b]	Lattice constant of CeO_2 (nm)	Fe_2O_3 crystallite size (nm)[b]	Ag crystallite size (nm)[b]	Fe/Ce ratio[c]
Fe-C	25.7			43		
Fe-R	19.2			56		
Fe-O	16.6			64		
Ag/Fe-C	19.5			46	5.4	
Ag/Fe-R	17.3			58	6.7	
Ag/Fe-O	17.1			62	7.3	
Fe@Ce-C	29.4	6.2	0.5397	44		0.85
Fe@Ce-R	24.5	6.1	0.5403	61		1.23
Fe@Ce-O	25.8	6.7	0.5408	67		1.43
Ag/Fe@Ce-C	27.1	6.4	0.5395	43	< 3	0.84
Ag/Fe@Ce-R	21.3	6.4	0.5402	60	< 3	1.23
Ag/Fe@Ce-O	24.7	6.6	0.5407	67	< 3	1.44

[a] External surface area obtained from N_2 physisorption tests at −196 °C.
[b] Calculated by Scherrer equation from the XRD data.
[c] Obtained from the ICP results (the sizes of Fe-C, Fe-R and Fe-O differed from each other, so different amount of CeO_2 was used to build similar CeO_2 coatings over them).

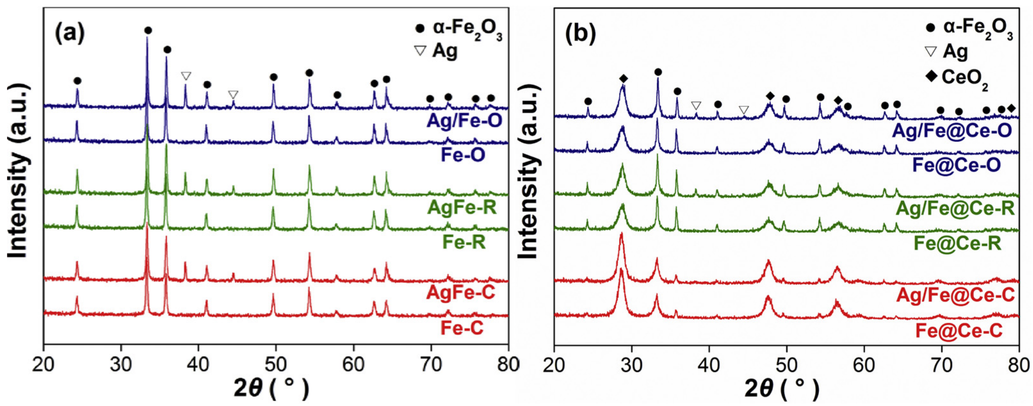

Fig. 2. XRD patterns of different catalysts (a) without or (b) with CeO_2.

larger than 2 nm) were similar and relatively low (< 30 m^2/g). CeO_2 coating led to extra intra-particle voids and increased the S_{Ext} of Fe@Ce and Ag/Fe@Ce to some extent. Anyhow, given soot particles (≥ 25 nm) are always too large to enter catalysts' mesopores, the number of catalyst-soot contact points instead of S_{Ext} plays real important role for soot catalytic oxidation [6].

Based on the morphology of different catalysts, a primary estimation of the catalyst-soot contact conditions was given (see the Supporting Information for more details). Briefly, cube-like catalysts exhibited higher outer surface area (S_{Out}) and thus more catalyst-soot contact points than the other two series of catalysts. This might cause further influences on their catalytic performance, which would be discussed later.

3.2. Chemical states and surface oxygen vacancies

XPS was performed to monitor the chemical states of the catalysts. Some of the spectra had been normalized in intensity to allow for a better comparison of the shape and intensity of the peaks. As shown in Fig. 3a and b, all the catalysts exhibited the Fe $2p_{3/2}$ peak and the corresponding satellite peak at 711.2 eV and 719.4 eV, respectively, indicating their Fe_2O_3 surface was dominated by Fe^{3+}. Interestingly, the satellite peak corresponding to Fe^{2+} (716.0 eV) could be observed only when there was CeO_2 in the catalysts (Fe@Ce and Ag/Fe@Ce) [31,32]. This indicated that Fe^{2+} sites were created via the interaction between Fe_2O_3 and CeO_2, probably through an interfacial redox process: $x Fe_2O_3 + (2\text{-}y) CeO_{2\text{-}x} \rightarrow x Fe_2O_{3\text{-}y} + (2\text{-}y) CeO_2$ [15,18]. Notably, Fe@Ce-C and Ag/Fe@Ce-C exhibited obviously more Fe^{2+} species than other samples, suggesting there was strong Fe_2O_3-CeO_2 interfacial interaction over these cube-like catalysts (no deconvolution of the Fe_2O_3 XPS spectra were made, since it was too subjective and relied strongly on estimation of the background) [32]. Moreover, since the creation of surface oxygen vacancies ($V_{O\text{-}s}$) was closely related with the presence of Fe^{2+} [29], there should be much more $V_{O\text{-}s}$ on the Fe_2O_3 surface of Fe@Ce and Ag/Fe@Ce than on Fe and Ag/Fe, respectively.

As shown in Fig. 3c, Ce^{3+} cations gave rise to four satellite peaks labeled as u°, u′, v° and v′. All the Fe@Ce and Ag/Fe@Ce catalysts exhibited similar surface Ce^{3+} content (Ce^{3+}/Ce^{4+} ≈ 0.38) and thus identical $V_{O\text{-}s}$ over the CeO_2 layers [6–9]. Ag in all the samples exhibited Ag $3d_{5/2}$ binding energies at ~368.1 eV and a splitting of 6 eV (Fig. 3d), indicating the metallic nature of these silver species [6,7]. These results agreed well with the HRTEM and XRD results.

3.3. Soot oxidation activities

Temperature programmed oxidation (TPO) is an important method which helps to bridge the gap between exploratory studies and on-the-road tests of soot catalytic oxidation [5]. Herein, by using T_{50} (temperatures at which 50% soot were converted into CO_x) as comparison criteria, the activity of different Fe_2O_3-based catalysts are illustrated and compared with the highly active cube-like CeO_2 (Ce-C) and Ag/CeO_2 (Ag/Ce-C) catalysts (see Figs. S2 and S3 for details) [6,7]. All the catalysts yielded a high CO_2 selectivity during the reaction (CO_2/CO_x > 99%).

As shown in Fig. 4a, under the "tight" contact mode, Ce-C exhibited better activity than all the Fe_2O_3 catalysts ($\triangle T_{50}$ = 30 ~ 50 °C), while Fe-O was more active than Fe-C and Fe-R. With the assistance of Ag particles, the Ag/Fe catalysts showed higher activity than Fe_2O_3, but they were still worse soot oxidizers compared with Ce-C. By contrast, the promotion of CeO_2 coating on Fe_2O_3 was highly significant. The T_{50}s of Fe@Ce were at least 20 °C lower than that of Ce-C. Loading silver on Fe@Ce gave rise to catalysts with comparable (Ag/Fe@Ce-O and Ag/Fe@Ce-R) or better (Ag/Fe@Ce-C) activity than Ag/Ce-C. Given that Ag supported on cube-like CeO_2 was among the most active soot oxidation catalysts under simulative CGPF conditions [4], the practical potential of Ag/Fe@Ce catalysts was considerably high.

More "practical" results are illustrated in Fig. 4b. In the "loose" contact mode, a lot of the reactive sites on catalyst surface cannot participate in the reaction because they are too far away from soot [29]. Consequently, Ce-C and Ag/Ce-C with high catalyst outer surface area (Supporting Information) lost their superiority partially. The T_{50} gap between Ce-C and the Fe_2O_3 catalysts was only about 20 °C, and all the Ag/Fe@Ce catalysts ignited soot at much lower temperatures than Ag/Ce-C. Notably, contrary to the results in Fig. 4a, the Ag/Fe catalysts (especially Ag/Fe-C) showed remarkably better activity than Fe@Ce in the "loose" contact mode. In sum, the Ag/Fe@Ce soot oxidation catalysts showed higher practicability than Ag/Ce-C, and the modification with either Ag or CeO_2 could make Fe_2O_3 more practical than Ce-C.

As shown in Fig. S3b, introducing additional O_2 (e.g. 10%) could increase the catalysts' activity to a large extent. In addition, the water vapor—which exists commonly in mobile exhaust—could further accelerate soot combustion over the Ag/Fe@Ce catalysts. For example, as shown in Fig. 4b, with the introduction of 5% H_2O, the T_{50} of Ag/Fe@Ce-O decreased about 30 °C. Such an obvious promotion of water on soot oxidation over Ag/CeO_2 catalysts had been attributed to the elimination of adsorbed hydrogen by oxygen species and/or the increase in contact area caused by gasification of carbon with water [7]. These results confirmed the ultrahigh practical potential of Ag/Fe@Ce catalysts for soot combustion. Notably, since almost all of the characterizations applied in this work (e.g. HRTEM, XRD, XPS, Raman, TGA and especially H_2-TPR) could not be performed in a humid atmosphere, detailed mechanism exploration will be made based on soot oxidation reactions in absence of water.

Given soot oxidation is a solid-solid catalytic reaction, the influences of catalyst morphology and heat/mass transfer limitations during TPO tests make it difficult to compare the catalysts' intrinsic activity

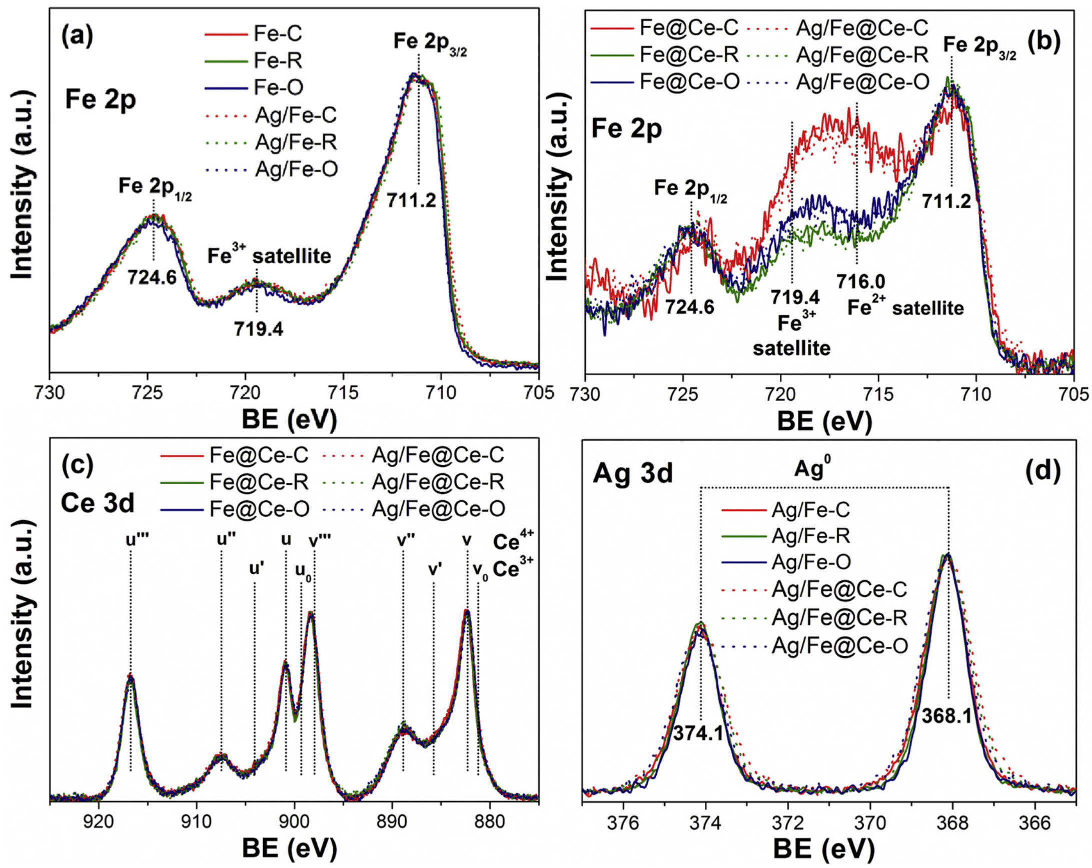

Fig. 3. XPS spectra of the catalysts in the (a, b) Fe 2p, (c) Ce 3d and (d) Ag 3d core level regions.

according to the above results. Therefore, quantitative comparison was made based on steady-state measurements under the "tight" contact mode, during which the interference of catalyst-soot contact condition was excluded (details about normalization of contact conditions are shown in Scheme. S2). At 250 °C, all the catalysts were inert except for Ag/Fe@Ce and Ag/Ce-C. As shown in Fig. 5a, Ag/Fe@Ce-C following by Ag/Fe@Ce-O and Ag/Fe@Ce-R exhibited extremely high intrinsic activity (3, 2.2 and 1.9 times higher than Ag/Ce-C, respectively). This result implied the ability of Ag/Fe@Ce catalysts for soot ignition at ultra-low temperature (≤ 250 °C). After being heated to 275 °C, Fe@Ce and Ce-C started to ignite soot. Their intrinsic activities followed an order of Fe@Ce-C > Fe@Ce-R > Fe@Ce-O > Ce-C (Fig. 5b). The Ag/Fe catalysts were not active until the temperature reached 300 °C, and all of them exhibited severe deactivation during the reaction (Fig. 5c). Similar deactivation could not be observed over Fe@Ce-O at the same temperature. We previously evidenced that this deactivation came from insufficient O_x^- (especially O_2^-) supplement [6–9]. Thus, Ag/Fe seemed to be an inefficient O_x^- supplier compared with Fe@Ce. Finally, at 325 °C, all the Fe_2O_3 catalysts were activated. From Fig. 5d, it can be seen that Fe-C and Fe-R showed identical intrinsic activity, both were much less active than Fe-O. Notably, Ce-C was still far more active than all these Fe_2O_3 samples though it exhibited some deactivation [6]. All the above data was generally in line with the soot-TPO results obtained in the "tight" contact mode (Fig. 4a).

In addition, we measured morphology of the catalysts after the steady-state reactions at 325 °C. As shown in Fig. S4, all the Fe, Fe@Ce and Ag/Fe@Ce catalysts preserved their original morphologies, while silver agglomerated into large particles over the Ag/Fe catalysts. These aggregated Ag particles were always found staying close to soot (Figs. S4b, S4f and S4j). Some of them even broke away from the Fe_2O_3

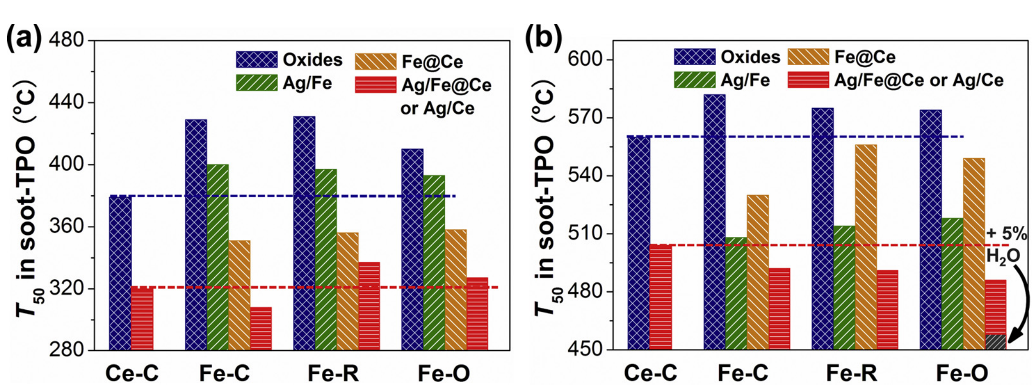

Fig. 4. Temperatures at which 50% soot were converted into CO_x (T_{50}) during soot temperature-programmed oxidation (TPO) reactions under (a) "tight" contact and (b) "loose" contact. Reaction conditions: 1% O_2/N_2 (500 ml/min), heating rate = 5 °C/min, catalyst/soot = 10/1.

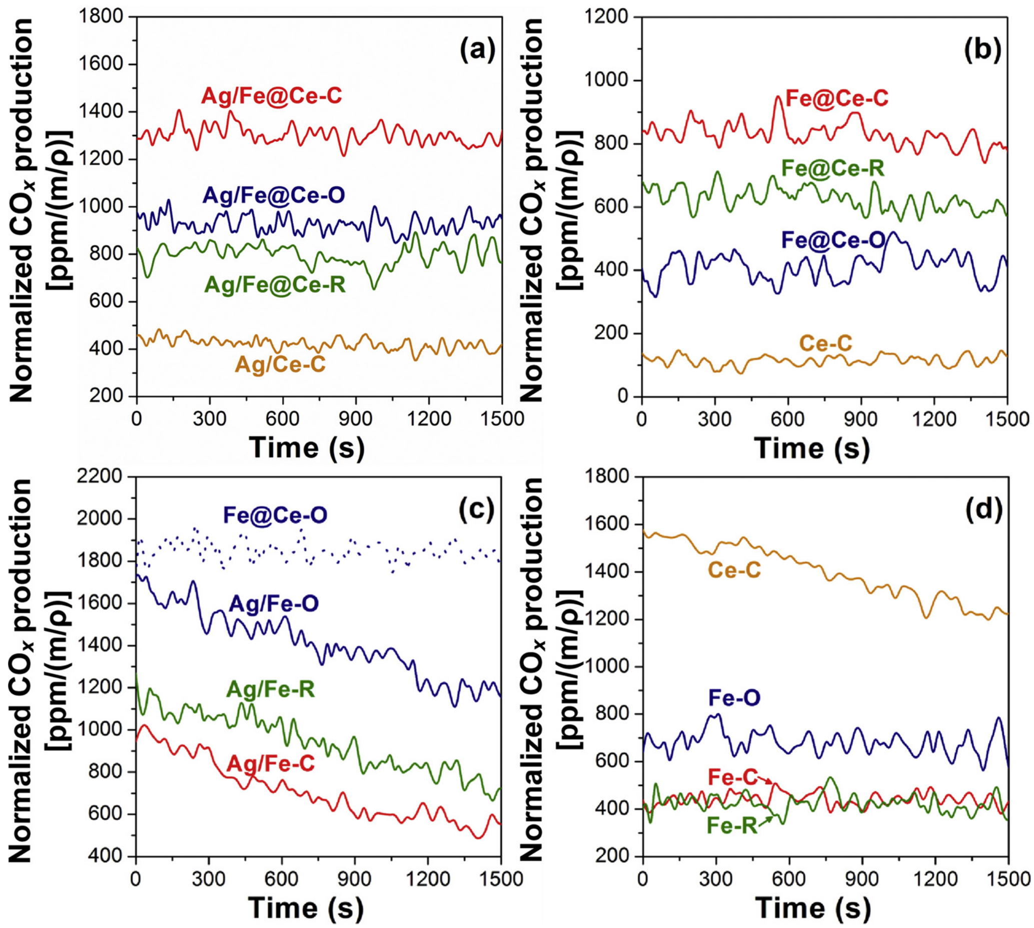

Fig. 5. CO_2 concentration (normalized by the available number of catalyst-soot contact points) during isothermal soot oxidation at (a) 250 °C, (b) 275 °C, (c) 300 °C and (d) 325 °C. Reaction conditions: 1% O_2/N_2 (500 ml/min), catalyst/soot = 10/1, "tight" contact.

supports and were enwrapped with soot completely (Fig. S5). Similar results about the move and redispersion of silver during soot oxidation have been reported over Ag/SiO_2 and Ag/Al_2O_3 catalysts [33,34], suggesting a weaker interaction between Ag-Fe_2O_3 than Ag-CeO_2 [6]. The migration of silver favored its contact with soot, resulting in enhanced activity of the Ag/Fe catalysts in the "loose" contact mode (Fig. 4b). While if they were mixed with soot tightly, influence of catalysts' intrinsic activity overwhelmed factors like active oxygen delivery (catalyst → soot) and molten silver wetting/spreading, resulting in their relatively poor performance. Notably, this Ag sintering might contribute to deactivation of the Ag/Fe catalysts with time on stream, as indicated in Fig. 5c [7].

3.4. "Active oxygen" on the catalysts

It has been widely accepted that the catalytic oxidation of soot depends crucially on the participant of O_x^- species (x = 1 or 2, the so-called "active oxygen") [5–10]. In this study, Raman was applied to detect and distinguish O_x^-. According to earlier works, the bands in the ranges of 1158–1126 cm^{-1} can be attributed to superoxide complexes (O_2^-), while peroxide (O_2^{2-}) gives rise to bands at 964–951 cm^{-1} and 883–825 cm^{-1} [35,36]. As shown in Fig. 6, Fe-C, Fe-R and Fe-O exhibited the signals of both types of O_x^-, and Fe-O possessed more O_2^- than the other two catalysts. The introduction of Ag only increased the O_2^- content slightly. After coating with CeO_2, the Fe@Ce catalysts showed slightly more O_2^- than their Fe_2O_3. Impregnation of Ag on these Fe@Ce catalysts further conferred more O_x^-. Specifically, Ag/Fe@Ce-C possessed high content of both O^- and O_2^-, indicating an effective Ag-assisted O_x^- generation process [10].

Besides O_x^-, some bulk information of Fe_2O_3 and CeO_2 could also be revealed by Raman spectra. As shown in Fig. 6, on one hand, the six characteristic peaks of hematite in the range of 200 ~ 1400 cm^{-1} confirmed the presence of α-Fe_2O_3 [31], which was in accordance with the XRD results. On the other hand, the intensity ratio of ceria defect-induced (D, ~600 cm^{-1}) and F_{2g} mode (~465 cm^{-1}) peaks (I_D/I_{F2g}) demonstrated the bulk oxygen vacancies ($V_{O\text{-}b}$) of CeO_2 [7]. Clearly, Fe@Ce-C exhibited lower I_D/I_{F2g} than Fe@Ce-R and Fe@Ce-O, indicating there were less $V_{O\text{-}b}$ in the bulk phase of CeO_2 in the cube-like catalysts (no quantitative analysis was made, because it was too subjective to make subtraction of the Fe_2O_3 background). This was attributed to the stronger interfacial interaction between Fe_2O_3 and CeO_2 ($x Fe_2O_3 + CeO_{2\text{-}x} \rightarrow 2x FeO + CeO_2$) in this sample than others, which had already been evidenced by the XPS results.

3.5. Generation and regeneration of "active oxygen"

H_2-TPR is a well established method to investigate catalyst redox properties and the generation/regeneration of O_x^-. During the H_2-TPR tests, all the Fe_2O_3 catalysts exhibited similar H_2 consumption profiles (Fig. 7a), with a sharp reduction peak at 310 °C ($Fe_2O_3 \rightarrow Fe_3O_4$) and a broad peak at around 550 °C ($Fe_3O_4 \rightarrow FeO \rightarrow Fe$) [37]. The similarity in bulk reduction of Fe-C, Fe-R and Fe-O implied that, the different soot oxidation activities of these Fe_2O_3 catalysts came from their different surface structure [38]. For the Ag/Fe_2O_3 catalysts, the H_2 spillover effect caused by silver shifted both these reduction peaks towards low temperatures but did not reshape them (Fig. 7b) [6]. It is worth noting that, the Fe_2O_3 catalysts were reduced into Fe_3O_4 completely after the first H_2 consumption peak (~330 °C, see Fig. S6a). Nevertheless, all the

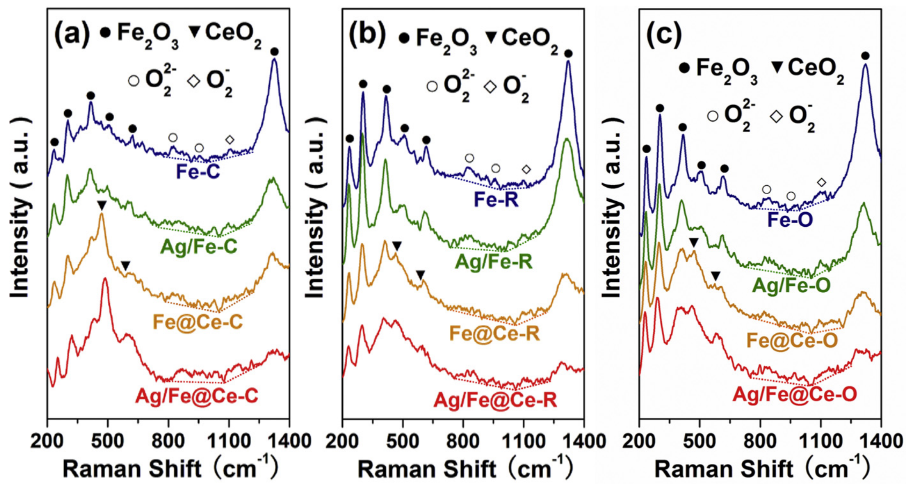

Fig. 6. Raman spectra of the (a) cube-like, (b) rhombohedron-like and (c) octadecahedron-like catalysts.

Fe_2O_3-based catalysts remained their original phases (α-Fe_2O_3) after reacting with soot isothermally at 325 °C (Figs. S6b, S6c and S6d). Therefore, it was incorrect to build direct relationship between the catalysts' soot oxidation activity and their reducibility obtained from the Fe_2O_3-H_2 reaction. In contrast, monitoring the generation/regeneration of O_x^- by combining oxidation and reduction treatments gave better understanding about the reactive phases for soot catalytic oxidation [6–9].

From the H_2-TPR profile of Fe@Ce-C in Fig. 7c, it can be seen that the reduction peak at 317 °C ($Fe_2O_3 \rightarrow Fe_3O_4$) exhibited a shoulder at around 275 °C, which was assigned to surface O_x^- species over the polycrystalline CeO_2 layer [6]. Additional O_x^- generated after the preoxidation treatment (see the "O_2-1 st" curve). After this TPR process, a subsequent oxidation treatment reshaped the H_2 consumption peaks. See for the "O_2-2nd" test, the Fe_2O_3-derived peak shifted to 233 °C, probably because of the formation of easily-reduced surface hydroxyl groups and $V_{O\text{-}s}$ [37]. Meanwhile, a relatively high amount of surface O_x^- (~275 °C) was detected, which indicated that the active oxygen species can be regenerated rapidly by O_2 over this catalyst [6–8]. Due to the weaker Fe_2O_3-CeO_2 interaction, Fe@Ce-R (Fig. 7d) and especially Fe@Ce-O (Fig. 7e) showed much more difficult generation and regeneration of O_x^- compared with Fe@Ce-C.

After Ag loading, the catalysts' redox ability changed remarkably. As shown in Fig. 7f, all the reduction peaks in H_2-TPR shifted to temperatures lower than 300 °C due to H_2 spillover on Ag. Specifically, the amount of O_x^- raised significantly over Ag/Fe@Ce-C (~690 $\mu mol_{H2}/g_{cat.}$, see Fig. S7 for deconvolution details) compared with Fe@Ce-C (~106 $\mu mol_{H2}/g_{cat.}$), which agreed well with the Raman results (Fig. 6a). Since silver in the as-received catalysts presented in the metallic form, this increase in O_x^- came from not the O_2 activation on Ag, but the pumpout of catalysts' bulk oxygen (from CeO_2 and Fe_2O_3) by silver [6,7]. As shown in Fig. 7g and h, comparing with Ag/Fe@Ce-C, Ag/Fe@Ce-R and Ag/Fe@Ce-O exhibited obviously lower content of O_x^- (236 and 170 $\mu mol_{H2}/g_{cat.}$, respectively). This could be attributed to their relatively weak O_x^- generation ability and/or small CeO_2 contents (Table 1).

The cycled reduction/oxidation processes resulted in distinct reduction peaks assigning to surface O_2^- (0–40 °C), O^- (50–70 °C) and O^{2-} (100–240 °C) (see the "O_2-2nd" curve) [7]. During these tests with O_2 pretreatment at elevated temperatures, it is possible for Ag to be activated and react with O_2 ($xO_2 + 2Ag \rightarrow 2Ag^+ + 2O_x$-), resulting in formation of Ag-O_x- species. Therefore, the O_x- detected in "O_2-1 st" and "O_2-2nd" tests may be contributed by both CeO_2 and silver. Notably, the oxidation of silver particles should be limited to their surface (chemisorbed oxygen and/or surface Ag_xO). This is because even after reactions in 1% O_2 at 325 °C, silver species still remained as Ag° instead of Ag_xO particles (Figs. S4 and S5). Moreover, even for Ag/CeO_2 with detectable Ag_xO species, the total contribution of Ag_xO to H_2 consumption was still negligible [7], so the total amount of Ag-O_x- in the current study is expected to be low.

Wherever the O_x^- species came from, they (especially O_2-) were proven highly active for soot catalytic oxidation [4–11]. During the "O_2-1 st" tests, O_2- species was observed over Ag/Fe@Ce-C and Ag/Fe@Ce-O but not over Ag/Fe@Ce-R. This indicated that the activation of Ag/Fe@Ce-R was more difficult than its two counterparts, which was in line with its relatively low soot oxidation activity (Figs. 4a and 5a). All the Ag/Fe@Ce catalysts generated certain amount of O_2- after extra redox cycles (see the "O_2-2nd" curves in Fig. 7f, g and h), implying their good redox stability. These results agreed well with the stable catalytic performance of Ag/Fe@Ce during the isothermal soot oxidation reactions (Fig. 5).

3.6. Consumption of "active oxygen"

Given the reoxidation of oxygen vacancies (V_O) is much faster than V_O generation [38], the supply and consumption of catalysts' oxygen species may be even more important than the regeneration of them during soot oxidation reactions. Although the TPR results unraveled the generation/regeneration of surface O_x^-, quantitative information about catalysts' oxygen consumption rate could only be given by OSC tests. Fig. 8 illustrates the catalyst weight change under oscillating feedstream conditions. It is worth noting that, even for Ag/Fe@Ce with the most abundant surface O_x^- among all the catalysts (Figs. 6 and 7), O_x^- species made up only 0.97% of its total weight (609 μmol O/$g_{cat.}$). The O_x^- content of the other catalysts was always below 0.4 wt.%. Therefore, catalysts' weight losses (> 1.2 wt.% for Ag/Fe@Ce-C, > 0.8 wt.% for other catalysts) in the reductive atmosphere (1% H_2/N_2) came from oxygen consumption both on surface (CeO_2 and Ag) and in bulk (CeO_2 and/or Fe_2O_3) of catalysts.

Among the three Fe_2O_3 catalysts, Fe-O consumed H_2 slightly faster than Fe-C and Fe-R did (see the slope of the first weight loss process). After coating with CeO_2, the oxygen consumption rate of Fe@Ce-C increased significantly, while promotion of CeO_2 on Fe@Ce-R and Fe@Ce-O was not so obvious. These results agreed with the catalysts' soot oxidation activity (Fig. 5b), indicating Fe@Ce-C exhibited rapid migration of bulk oxygen [14]. The efficiency of oxygen delivery could be further improved by Ag loading. As shown in Fig. 8, Ag/Fe@Ce-C exhibited the highest oxygen delivery rate, followed by Ag/Fe@Ce-O and Ag/Fe@Ce-R. In sum, for all the catalysts, their oxygen delivery efficiency followed an order of Ag/Fe@Ce > Fe@Ce > Fe.

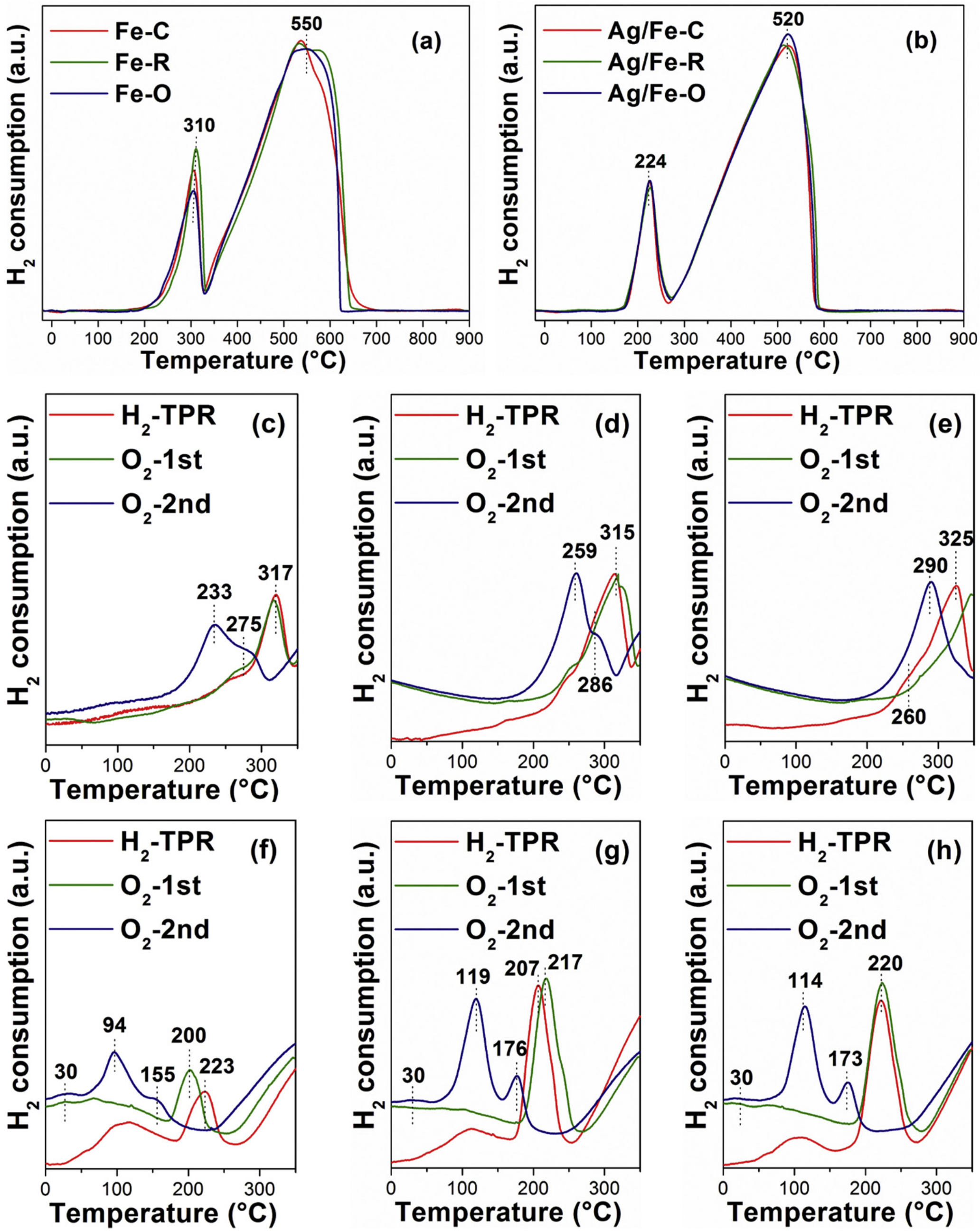

Fig. 7. H_2-TPR results of the (a) Fe_2O_3 and (b) Ag/Fe_2O_3 catalysts. H_2-TPR and cycled TPR results of (c) Fe@Ce-C, (d) Fe@Ce-R, (e) Fe@Ce-O, (f) Ag/Fe@Ce-C, (g) Ag/Fe@Ce-R and (h) Ag/Fe@Ce-O.

It should be noted that, Ag nano-particles influenced the oxygen delivery of Fe_2O_3 and CeO_2 in different ways. As shown in Fig. 8d, Ce-C showed rapid but small weight oscillation (maximum weight loss ~0.1 wt.%, $CeO_2 \leftrightarrow CeO_{1.98}$), the loading of silver doubled its oxygen supply, suggesting a deeper utilization of the CeO_2 bulk oxygen [6,7]. In contrast, Ag/Fe-C exhibited slower oxygen consumption than Fe-C. This difference indicated the different interactions between Ag-CeO_2 and Ag-Fe_2O_3, which would be discussed further.

4. Discussion

As is well known, the catalytic oxidation of soot mainly follows a Mars-van-Krevelen-like mechanism, in which the surface oxygen species (O_x^-, especially O_2^-) are continually consumed by soot and regenerated via gaseous O_2 and catalyst bulk oxygen. During a typical catalytic cycle, the generation/regeneration of O_x^- and their transfer onto soot are the most crucial steps which determine the activity of catalysts [4–10]. In this work, the above steps were influenced by the morphology-controlled Fe_2O_3 (the "core"), the Ag/CeO_2 materials (the "shell") and their interaction, which will be discussed separately as following. Notably, given the catalysts' intrinsic activity could only be revealed by the results from steady-state measurements under the "tight" contact mode (Fig. 5). Most of the following discussion was based on these data.

4.1. The role of Fe_2O_3 crystal plane on soot oxidation

As indicated by the H_2-TPR and OSC results, Fe-C, Fe-R and Fe-O exhibited similar bulk reducibility (Fig. 7a), and the bulk migration of oxygen in Fe_2O_3 was rather slow (Fig. 8) [14,15]. Therefore, as has

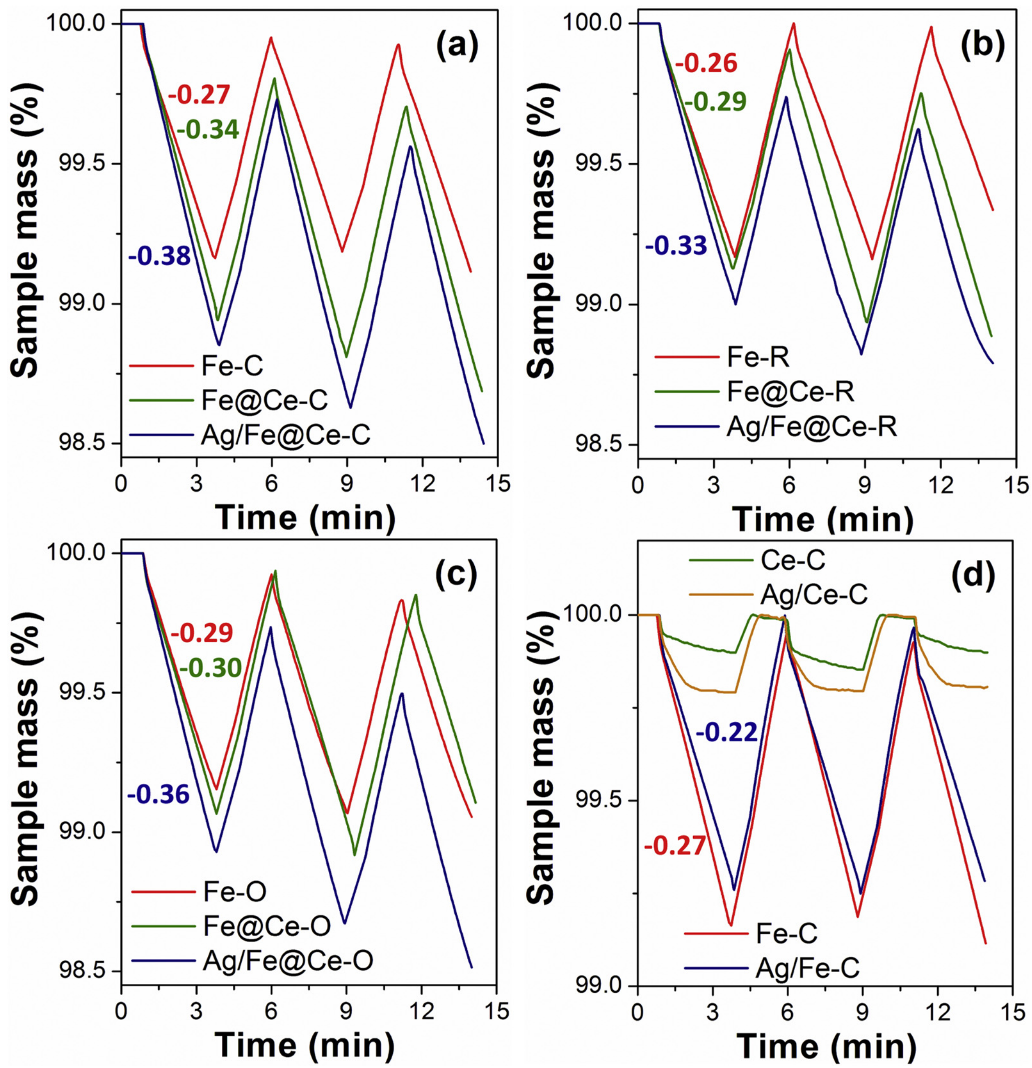

Fig. 8. Weight changes of different catalysts under cycled feed streams of 1% H_2/N_2 (~3 min) and 1% O_2/N_2 (~3 min) at 500 °C. The slope of the first weight loss process for each catalyst was labeled besides the profiles.

been evidenced by Mul et al. [39], the catalytic behavior of Fe_2O_3 should be determined mainly by their surface structure. As shown in Fig. 6, Fe-O (exposing mainly {113} planes) showed larger contents of highly active O_2^- than Fe-C and Fe-R (exposing either {012} or {014} planes). This abundance of surface-chemisorbed oxygen over Fe-O was reconfirmed by the O 1 s XPS spectra (Fig. S8). Consequently, the intrinsic catalytic activity of Fe-O was obviously higher than its counterparts (Fig. 5d). Based on the above results, it was suggested that the high-index {113} facets of α-Fe_2O_3 generated active oxygen more easily than the {012} and {014} planes, which thus conferred Fe-O high soot oxidation activity.

Why the {113} facets generated O_x^- readily? After excluding the effect of Fe_2O_3 bulk oxygen, the formation of O_x- should rely on the transformation of gaseous O_2: Fe^{2+}-$V_{O\text{-}s}$ + $x/2$ O_2 → Fe^{3+}-O_x^-. Clearly, this process is closely related to the concentration of electron-rich Fe cations. Similar to the results obtained by Chan et al. [40], the delicate difference in the surface Fe electronic states of Fe-O, Fe-C and Fe-R could not be observed by XPS (Fig. 3a). However, as illustrated in Fig. 9, based on charge-neutral stoichiometric "slices" through the bulk structure [39–42], the {012} facet of α-Fe_2O_3 is a corrugated surface with half singly coordinated oxygen atoms (O_I) and half triply coordinated oxygen atoms (O_{III}). While the {014} and {113} planes exhibit 1:1:1 and 1:1:2 ratios of singly (O_I), doubly (O_{II}), and triply (O_{III}) coordinated oxygen atoms, respectively. The surface Fe atoms coordinated to O_{II} have a bulk-like electronic structure, while the coordination with O_I and O_{III} result in Fe atoms in electron-poor and electron-rich states, respectively [39]. Therefore, the average Fe electronic state of the α-Fe_2O_3 {113} planes should be "richer" than that of the {012} and {014} planes. This inference was supported by both the DFT calculations of Chan et al. [39] and the ζ–potential results reported by Wang et al. [24]. As a consequence, for Fe-O enclosed mainly by the {113} planes, its O_x^- generation rate could be accelerated obviously.

After generation, the active oxygen species usually have to spillover some distance on catalyst surface before reaching the soot particles [11]. As we demonstrated earlier, excessive $V_{O\text{-}s}$ might transfer O_2^- into relatively inert O^- and O^{2-} during this process, which thus deactivates the ceria-based catalysts [6–8]. Nevertheless, due to the higher bond strength of Fe-O than Ce-O [43], the formation of surface oxygen vacancy is much more difficult over Fe_2O_3 (E_{vac} > 3 eV) than over CeO_2 (E_{vac} < 2.3 eV) [44,45]. Consequently, O_x- generation should be more rate-limiting than O_x- transformation for soot oxidation over Fe-C, Fe-R and Fe-O. This deduction was verified by the fact that catalyst deactivation—which was sensitive to O_x- transformation during spillover—did not occur during the steady-state soot oxidation tests of all the Fe_2O_3 catalysts (Fig. 5d). In sum, the electron-rich Fe cations on {113} facets influenced soot catalytic oxidation only in a positive way, which thus lead to the high intrinsic activity of Fe-O.

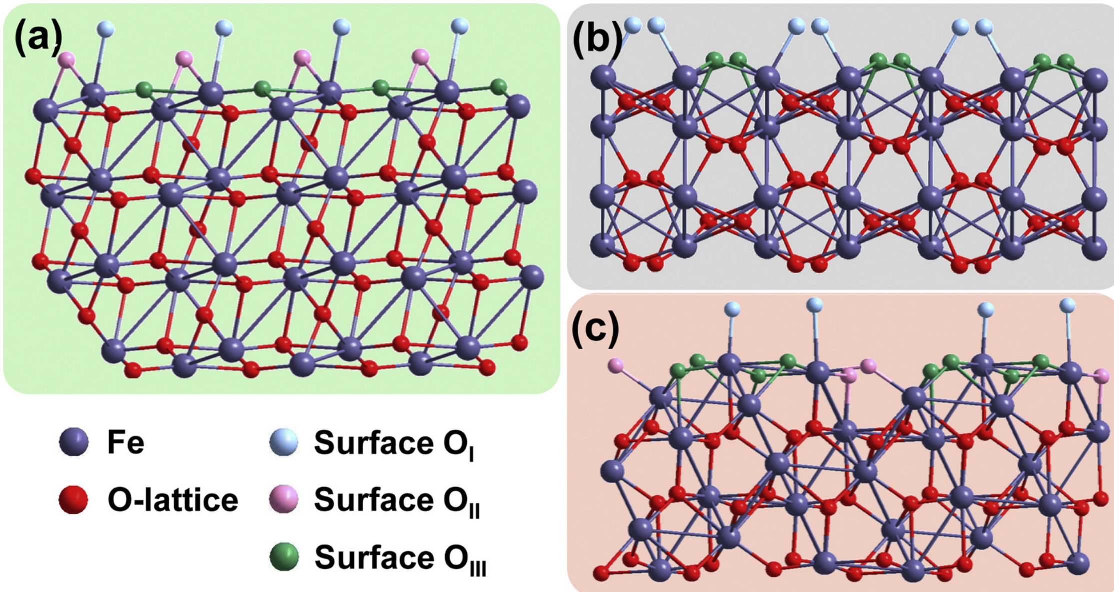

Fig. 9. Side views of optimized α-Fe_2O_3 (a) (014), (b) (012) and (c) (113) planes.

4.2. Effect of Fe_2O_3→CeO_2 oxygen delivery

As we reported previously, polycrystalline CeO_2 usually lacked the ability to supply active oxygen (especially O_2^-) continuously, which led to its deactivation for soot oxidation with time on stream [6,8]. In this study, however, no deactivation was observed over the Fe@Ce catalysts with outer layers consisted of polycrystalline CeO_2 (Fig. 5b). So, the inner α-Fe_2O_3 must have promoted the O_x^- supply of ceria in some way. As reported by Machida et al., because of the oxygen delivery between Fe_2O_3 and CeO_2, the CeO_2 particles loaded on Fe_2O_3 exhibited higher OSC than pure CeO_2 [14]. Similarly, the XPS results (Fig. 3b) indicated that, the strong Fe_2O_3-CeO_2 interaction in Fe@Ce catalysts led to transfer of oxygen from Fe_2O_3 to CeO_2. Another clue for this oxygen delivery is the relatively low content of oxygen vacancies in CeO_2. The Ce^{3+} content (Ce^{3+}/Ce^{4+} ≈ 0.38) of the polycrystalline CeO_2 layer in this study was much lower than that of the polycrystalline CeO_2 particles (Ce^{3+}/Ce^{4+} ≈ 0.57) we once reported [6]. This indicated that oxygen vacancies of the CeO_2 shells were re-filled readily by oxygen from the Fe_2O_3 cores. Consequently, the transformation of O_2^- [O_2^- (+$V_{O\text{-}s}$-e^-) → $2O^-$ (+2$V_{O\text{-}s}$-e^-) → $2O^{2-}$] during spillover was suppressed, resulting in good catalyst stability during the steady-state soot oxidation reactions [8].

More importantly, this Fe_2O_3→CeO_2 oxygen delivery opened an efficient route for "pumping" oxygen out of Fe_2O_3: Once surface oxygen vacancies generated over Fe_2O_3 in assistance of CeO_2 (Fig. 3b), oxygen in Fe_2O_3 bulk phase could diffuse onto the Fe_2O_3-CeO_2 interface to refill them. This process enhanced the utilization of oxygen in the Fe_2O_3 cores effectively, making all the Fe@Ce catalysts better oxygen contributors than Fe_2O_3 (Fig. 8). These interfacial oxygen species might further migrate into ceria grains and result in abundant ceria oxygen as the "raw material" for active oxygen formation [6], which not only generated plenty of O_x^- on their external surface (Fig. 6), but also facilitated the regeneration of O_x^- after redox cycles (Fig. 7c). With these O_x^- as active phases [10], all the Fe@Ce catalysts exhibited significantly higher soot oxidation activity than their corresponding Fe samples (Figs. 4 and 5).

It should be noted that, the surface diffusion of Fe atoms into CeO_2 (Table 1) might reconstruct the Fe_2O_3 surface, resulting in a similar Fe_2O_3-CeO_2 interfacial structure for all the Fe@Ce catalysts. As a result, differences in the intrinsic oxygen delivery ability of different Fe@Ce catlaysts were leveled to a large extent. This was evidenced by the OSC results (Fig. 8b and c), in which Fe@Ce-O exhibited only slightly faster bulk oxygen consumption than Fe@Ce-R. In this case, the amount of Fe_2O_3-CeO_2 contact points determined the Fe@Ce catalysts' apparent oxygen delivery ability. As evidenced by XRD results (Table 1) and the difference in S_{out} of Fe_2O_3 (Scheme. S2), Fe@Ce-C exhibited the largest Fe_2O_3-CeO_2 interfacial area among the Fe@Ce catalysts. As a result, it exhibited the stronger Fe_2O_3-CeO_2 interaction (Fig. 3b) and higher Fe_2O_3→CeO_2 oxygen delivery rate than Fe@Ce-R and Fe@Ce-O. Consequently, Fe@Ce-C showed a rather low content of $V_{O\text{-}b}$ in CeO_2 (Fig. 6), indicating the oxygen-rich state of its CeO_2 shell and thereby led to its superior soot oxidation activity (Fig. 5b).

4.3. Effect of Ag loading and tandem oxygen delivery

The influence of Ag loading was complex. On one hand, as indicated before, Ag affected the oxygen delivery of Fe_2O_3 and CeO_2 differently: The oxygen reverse spillover from CeO_2 to Ag improved the utilization of ceria bulk oxygen remarkably (Fig. 8d) [6,7,44]. The Raman results reconfirmed such an oxygen delivery process: As shown in Fig. 6 (detailed comparison in Fig. S9), the Ag/Fe@Ce catalysts (especially Ag/Fe@Ce-C and Ag/Fe@Ce-O) exhibited higher I_D/I_{F2g} than the Fe@Ce samples, which demonstrated the "pumpout" of bulk oxygen by Ag and thereby the formation of extra $V_{O\text{-}b}$ in CeO_2. Such a pumpout effect was confirmed by the H_2-TPR results (Fig. 7), which has also been discussed detailedly in previous works [6,7].

Contrarily, oxygen can hardly transfer from Fe_2O_3 to Ag. This is because the formation of surface oxygen vacancies—which is rate-determining for oxygen reverse spillover—is relatively difficult over Fe_2O_3 [43–45]. This reverse spillover is also energetically unfavorable, given ΔH^o (Ag_2O), -31.1 kJ/mol, is more than 26 times smaller than that of Fe_2O_3 (ΔH^o = -824.2 kJ/mol). As a result, Ag particles could hardly improve the oxygen utilization (Fig. 8d) and O_x^- generation (Fig. 6) over Ag/Fe. This low O_x^- generation ability worked in tandem with Ag sintering (Figs. S4 and S5) to deactivate these catalysts during soot oxidation reactions (Fig. 5c). Therefore, although the mobility of Ag particles on Fe_2O_3 conferred them high activity under the "loose" contact mode [33,34], Ag/Fe_2O_3 were actually ruled out as practical catalysts for long-term using. In a word, Ag loading benefited only the oxygen delivery of Ag/Fe@Ce, which made them better active oxygen contributors than the Fe@Ce and Ag/Fe catalysts (Fig. 8).

On the other hand, Ag nano-particles participated in not only the

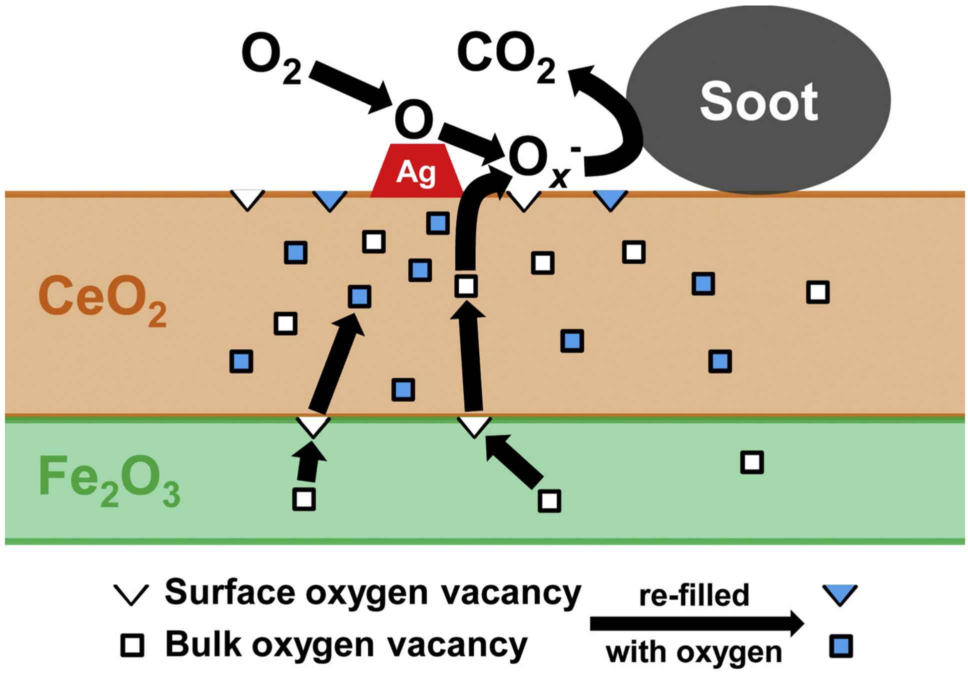

Fig. 10. Mechanism of soot oxidation over the Ag/Fe@Ce catalysts. Black arrows indicate the delivery of oxygen species.

bulk delivery of oxygen but also the activation of gaseous O_2, resulting in the continuous formation of O_x^- [6]. As indicated by the cycled TPR results (Fig. 7), among the Fe@Ce catalysts, only Fe@Ce-C exhibited relatively high O_x^- regeneration ability. In contrast, all the Ag/Fe@Ce catalysts gain more O_2^- after one reduction/oxidation cycle (comparing the "O_2-1 st" and "O_2-2nd" results). Given gaseous O_2 was the only oxidant for catalyst regeneration, one possible explanation was that the Ag nano-particles adsorbed and reduced O_2 directly ($Ag + O_2 \rightarrow Ag^+ + O_2$-). Meanwhile, Ag might also dissociate the gaseous O_2 into O [46], which further migrated onto the unsaturated CeO_2 support and transformed into O_x^- ($2O + Ce^{3+}\text{-}V_{O\text{-}s} \rightarrow Ce^{4+}\text{-}O_2^-$). Both these O_2 activation routes were supported by the first-principles calculations of Wang et al. [47] and were discussed detailedly in our earlier studies [6,7,9].

With the oxygen came from both the tandem $Fe_2O_3 \rightarrow CeO_2 \rightarrow Ag$ oxygen delivery and gaseous O_2 activation, the as-received Ag/Fe@Ce-C generated obviously more O_x^- (especially O_2^-) than Fe@Ce-C (see Figs. 6 and S10), and these O_x^- species could be regenerated easily once consumed during the redox cycles. In comparison, due to the limited Fe_2O_3-CeO_2 interface area and relatively small CeO_2 contents (Table 1), Ag/Fe@Ce-O and especially Ag/Fe@Ce-R exhibited less efficient utilization of active oxygen and thus worse soot oxidation activity than Ag/Fe@Ce-C. Based on the above discussion, a model about soot oxidation over the Ag/Fe@Ce catalysts was built and shown in Fig. 10.

5. Conclusions

In this study, by using α-Fe_2O_3 catalysts exposing different planes as the "core", a series of Ag promoted Fe_2O_3@CeO_2 core-shell catalysts were developed. Based on the structural properties and the intrinsic catalytic behavior of these model catalysts, conclusions can be drawn as:

(1) The soot oxidation activity of hematite surface facets followed the order of {113} > {014} ≈ {012}. The electron-rich state of the surface Fe atoms was behind the high content of O_x^- and the high activity of Fe_2O_3 {113} planes.
(2) A polycrystalline CeO_2 outer layer improved the oxygen utilization of Fe_2O_3 significantly. The oxygen delivery from Fe_2O_3 to CeO_2 resulted in fast generation of O_x^- and thus better soot oxidation activity of Fe_2O_3@CeO_2 than Fe_2O_3.
(3) Ag loading facilitated both the utilization of ceria bulk oxygen and the activation of gaseous O_2. With the $Fe_2O_3 \rightarrow CeO_2 \rightarrow Ag$ tandem delivery of oxygen, the Ag promoted Fe_2O_3@CeO_2 catalysts showed superior low temperature soot oxidation activity.

Based on these conclusions, it is suggested that the Ag/Fe_2O_3@CeO_2 materials are more promising catalyst than nano-cubic Ag/CeO_2 for CGPF. They outstand over Ag/CeO_2 in both the low-temperature soot oxidation activity and the cost-efficiency. Furthermore, we suppose this NM/TMO_x@CeO_2 (NM = noble metal, TM = transition metal) core-shell structure can be extended widely to different systems and provide practical catalysts with high oxidation activity at low temperature.

Acknowledgements

The authors would like to acknowledge the National Natural Science Foundation of China (Grant No. 51702304), the Natural Science Foundation of Shandong Province (Grant No. ZR2017BEM006), the Postdoctoral Science Foundation of Shandong Province (Grant No. 201601009), the China Science and Technology Exchange Center (Grant No. 2016YFE0126600), the National Key R&D Program of China (Project 2017YFC0211102 and 2017YFC0211202) and China Postdoctoral Science Foundation (Grant No. 2015M580607 and 2017T100516).

Appendix A. Supplementary data

Supplementary material related to this article can be found, in the online version, at doi:https://doi.org/10.1016/j.apcatb.2018.05.093.

References

[1] T. Johnson, SAE Technical Series Paper 2014-01-1491, (2014).
[2] H. Wang, M. Liu, Y. Ma, K. Gong, W. Liu, R. Ran, D. Weng, X. Wu, S. Liu, ACS Catal. 8 (2018) 2796–2804.
[3] D. López-González, M.N. Tsampas, A. Boréave, L. Retailleau-Mevel, M. Klotz, C. Tardivat, B. Cartoixa, K. Pajot, P. Vernoux, Top. Catal. 58 (2015) 1242–1255.

[4] S. Liu, X. Wu, D. Weng, R. Ran, J. Rare Earth. 33 (2015) 567–590.
[5] A. Bueno-López, Appl. Catal. B 146 (2014) 1–11.
[6] S. Liu, X. Wu, W. Liu, W. Chen, R. Ran, M. Li, D. Weng, J. Catal. 337 (2016) 188–198.
[7] Y. Gao, A. Duan, S. Liu, X. Wu, W. Liu, M. Li, S. Chen, X. Wang, D. Weng, Appl. Catal. B 203 (2017) 116–126.
[8] S. Liu, X. Wu, J. Tang, P. Cui, X. Jiang, C. Chang, W. Liu, Y. Gao, M. Li, D. Weng, Catal. Today 281 (2017) 454–459.
[9] H. Wang, S. Liu, Z. Zhao, X. Zou, M. Liu, W. Liu, X. Wu, D. Weng, Catal. Sci. Technol. 7 (2017) 2129–2139.
[10] M. Machida, Y. Murata, K. Kishikawa, D. Zhang, K. Ikeue, Chem. Mater. 20 (2008) 4489–4494.
[11] K. Krishna, A. Bueno-López, M. Makkee, J.A. Moulijn, Appl. Catal., B 75 (2007) 189–200.
[12] P. Stelmachowski, P. Legutko, A. Kopacz, T. Jakubek, P. Indyka, P. Pietrzyk, M. Wojtasik, J. Markowski, W. Krasodomski, L. Ziemiański, G. Żak, Z. Sojka, A. Kotarba, Appl. Catal., B 199 (2016) 485–493.
[13] Z. Zhang, R. Balasubramanian, Environ. Sci. Technol. 51 (2017) 4248–4258.
[14] M. Machida, T. Kawada, H. Fujii, S. Hinokuma, J. Phys. Chem. C 119 (2015) 24932–24941.
[15] Z. Zhang, D. Han, S. Wei, Y. Zhang, J. Catal. 276 (2010) 16–23.
[16] V.V. Galvita, H. Poelman, V. Bliznuk, C. Detavernier, G.B. Marin, Ind. Eng. Chem. Res. 52 (2013) 8416–8426.
[17] Y. Cheng, W. Song, J. Liu, H. Zheng, Z. Zhao, C. Xu, Y. Wei, E.J.M. Hensen, ACS Catal. 7 (2017) 3883–3892.
[18] Y. Luo, R. Chen, W. Peng, G. Tang, X. Gao, Appl. Surf. Sci. 416 (2017) 911–917.
[19] E. Aneggi, D. Wiater, C. de Leitenburg, J. Llorca, A. Trovarelli, ACS Catal. 4 (2013) 172–181.
[20] J. Ouyang, J. Pei, Q. Kuang, Z. Xie, L. Zheng, ACS Appl. Mater. Interfaces 6 (2014) 12505–12514.
[21] H. Liang, X. Jiang, Z. Qi, W. Chen, Z. Wu, B. Xu, Z. Wang, J. Mi, Q. Li, Nanoscale 6 (2014) 7199–7203.
[22] L. Wortmann, S. Ilyas, D. Niznansky, M. Valldor, K. Arroub, N. Berger, K. Rahme, J. Holmes, S. Mathur, ACS Appl. Mater. Interfaces 6 (2014) 16631–16642.
[23] R.D. Rodriguez, D. Demaille, E. Lacaze, J. Jupille, C. Chaneac, J. Jolivet, J. Phys. Chem. C 111 (2007) 16866–16870.
[24] C. Wang, J. Shi, X. Cui, J. Zhang, C. Zhang, L. Wang, B. Lv, J. Catal. 345 (2017) 104–112.
[25] M. Lin, L. Tng, T. Lim, M. Choo, J. Zhang, H.R. Tan, S. Bai, J. Phys. Chem. C 118 (2014) 10903–10910.
[26] J. Zhen, X. Wang, D. Liu, S. Song, Z. Wang, Y. Wang, J. Li, F. Wang, H. Zhang, Chem. Eur. J. 20 (2014) 4469–4473.
[27] Y. Kameya, K.O. Lee, J. Nanopart. Res. 15 (2013) 2006.
[28] T. Boger, D. Rose, P. Nicolin, N. Gunasekaran, T. Glasson, Emiss. Control Sci. Technol. 1 (2015) 49–63.
[29] J.P.A. Neeft, O.P. van Pruissen, M. Makkee, J.A. Moulijn, Appl. Catal. B 12 (1997) 21–31.
[30] J.A. Farmer, C.T. Campbell, Science 329 (2010) 933–936.
[31] Y. Ling, G. Wang, J. Reddy, C. Wang, J.Z. Zhang, Y. Li, Angew. Chem. Int. Ed. 51 (2012) 4074–4079.
[32] S. Song, J. Kim, D. Lee, J. Lee, T. Min, J. Chae, J. Bae, J. Lee, J. Lee, S. Park, J. Am. Ceram. Soc. 100 (2017) 3928–3934.
[33] K. Kamatani, K. Higuchi, Y. Yamamoto, S. Arai, N. Tanaka, M. Ogura, Sci. Rep. 5 (2015) 10161.
[34] Y. Gao, X. Wu, S. Liu, M. Ogura, M. Liu, D. Weng, Catal. Sci. Technol. 7 (2017) 3524–3530.
[35] H. Zhang, C. Wang, H. Sun, G. Fu, S. Chen, Y. Zhang, B. Chen, J.R. Anema, Z. Yang, J. Li, Z. Tian, Nat. Commun. 8 (2017) 15447.
[36] V.V. Pushkarev, V.I. Kovalchuk, J.L. d'Itri, J. Phys. Chem. B 108 (2004) 5341–5348.
[37] S. Gómez-Quero, F. Cárdenas-Lizana, M.A. Keane, J. Catal. 303 (2013) 41–49.
[38] L. Nie, D. Mei, H. Xiong, B. Peng, Z. Ren, X. Hernandez, A. DeLaRiva, M. Wang, M.H. Engelhard, L. Kovarik, A.K. Datye, Y. Wang, Science 358 (2017) 1419–1423.
[39] G. Mul, F. Kapteijn, C. Doornkamp, J.A. Moulijn, J. Catal. 179 (1998) 258–266.
[40] J.Y.T. Chan, S.Y. Ang, E.Y. Ye, M. Sullivan, J. Zhang, M. Lin, Phys. Chem. Chem. Phys. 17 (2015) 25333–25341.
[41] S. Chatman, P. Zarzyckib, K.M. Rosso, Phys. Chem. Chem. Phys. 15 (2013) 13911–13924.
[42] V. Barrón, J. Torrent, J. Colloid Interface Sci. 177 (1996) 407–410.
[43] H. Idriss, E.G. Seebauer, Catal. Lett. 66 (2000) 139–145.
[44] S. Hu, Y. Wang, W. Wang, Y. Han, Q. Fan, X. Feng, Q. Xu, J. Zhu, J. Phys. Chem. C 119 (2015) 3579–3588.
[45] S.W. Hoh, L. Thomas, G. Jones, D.J. Willock, Res. Chem. Intermed. 41 (2015) 9587–9601.
[46] N. Severin, S. Kirstein, I.M. Sokolov, J.P. Rabe, Nano. Lett. 9 (2009) 457–461.
[47] J. Wang, M. Liu, M.C. Lin, Solid State Ionics 177 (2006) 939–947.